Micro-Doppler and Micro-Range Detection via Doppler-resilient 802.11ad-Based Vehicle-to-Pedestrian Radar

Gaurav Duggal[1], Shobha Sundar Ram[1] and Kumar Vijay Mishra[2]

[1]Indraprastha Institute of Information Technology Delhi, New Delhi 110020 India
[2]IIHR - Hydroscience & Engineering, The University of Iowa, Iowa City 52242 USA
E-mail: {gaurav17091, shobha}@iiitd.ac.in, kumarvijay-mishra@uiowa.edu

***Abstract*—We present a vehicle-to-pedestrian (V2P) link based on IEEE 802.11ad protocol for enhanced micro-Doppler and micro-range detection of targets such as pedestrians and cars. The 802.11ad preamble encapsulates complementary Golay sequences whose perfect autocorrelation property has been exploited recently for target localization in joint radar-communications systems. However, this property is perturbed by non-zero Doppler phase shifts introduced by moving targets. In this work, we propose embedding the 802.11ad packets with the Doppler-resilient waveforms based on the Prouhet-Thue-Morse sequence to improve the V2P target detection and recognition. We use analytical and animation models to generate the range-Doppler, range-time and Doppler-time radar signatures and compare them for standard and Doppler-resilient 802.11ad waveforms. Our numerical experiments for a pedestrian and a car show very detailed features with 20 dB improvement in sidelobe levels for a Doppler-tolerant link when compared with a standard 802.11ad protocol.**

***Index Terms*—automotive radar, Doppler resilient, Golay sequences, IEEE 802.11ad, micro-Doppler, vehicle-to-pedestrian radar**

I. Introduction

Lately, autonomous vehicles or self-driving cars have been witnessing enormous development in vehicular control [1], environmental sensing [2], in-vehicle entertainment [3], efficient resource utilization [4], and inter-vehicular synchronization [5]. An ongoing challenge is pedestrian detection and recognition in order to avoid road accidents and boost automotive safety. Conventional pedestrian detection techniques use sensors such as lidar [6], camera [7] and infrared/thermal detectors [8]. However, only radar offers the advantage of robust detection in adverse vision and weather conditions [9]. In this work, we focus on radar detection of pedestrians and cars.

Although targets such as pedestrians and cyclists have relatively smaller radar cross-section (RCS) and low mean Doppler velocity, they have informative signatures that are useful for classification [10]. Besides the translational motion, backscatter of these targets exhibit *micro-motions* generated by the non-rigid body parts. Examples include the swinging motion of the human arms and legs, and the rotation of the wheels of a car or bicycle. While the *micro-Doppler* features in these echoes are usually detected in joint time-frequency transforms, the *micro-range* features are captured in high range-resolution profiles [11]. In this context, millimeter-wave (mmWave) automotive radars operating at 77 GHz are increasingly the preferred technology because they are characterized by wide bandwidths (~4-7 GHz) and, hence, very high range resolution [12].

A concurrent development in intelligent transportation systems is the evolution of various vehicle-to-X (V2X) communication frameworks including vehicle-to-vehicle (V2V), vehicle-to-infrastructure (V2I), and vehicle-to-pedestrian (V2P) paradigms [13]. The overarching objective of these frameworks is to encourage sharing of road and vehicle information for applications such as environmental sensing, collision avoidance, and pedestrian detection. In the mmWave band, the 802.11ad protocol at unlicensed 60 GHz has been identified as a potential candidate for these communications because of high throughput advantages arising from wide bandwidth [14].

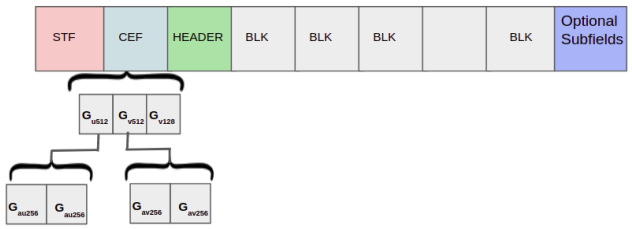

Fig. 1. Structure of the SCPHY IEEE 802.11ad frame which consists of the preamble (CEF and STF), a header, data blocks (BLK) and optional training fields.The CEF contains G_{u512}, G_{v512} each of which contains a 256 length Golay complementary pair.

More recently, there is active research thrust towards combining automotive radar and communication functionalities on a single carrier 802.11ad wireless framework; the primary benefits being sharing of the common spectrum and hardware resources. The 802.11ad-based V2V joint radar-communications (JRC) was proposed in [15, 16]. The corresponding V2I application has been explored recently in [17, 18] for radar-aided beam alignment to improve mmWave V2I communications. Contrary to these works, in this paper, we consider a V2P JRC scenario based on 802.11ad link for micro-Doppler detection.

The physical layer of IEEE 802.11ad protocol transmits control (CPHY), single carrier (SC) and orthogonal frequency-division multiplexing (OFDM) modulation frames at chip rates of 1.76 GHz and 2.64 GHz, respectively. Every single CPHY and SCPHY frame is embedded with a short training field (STF), a channel estimation field (CEF), header, data and a beamforming training field (see Fig. 1). The CEF consists of two 512-point sequences $Gu_{512}[n]$ and $Gv_{512}[n]$ which encapsulate *Golay complementary pairs* [19]. These paired sequences have the property of perfect *aperiodic* autocorrelation which is beneficial for communication channel estimation [20] and radar remote sensing [15]. The V2V JRC in [15] exploited the 802.11ad SCPHY Golay complementary pairs to estimate the ranges and Dopplers of simple *point* targets. This representation based on Swerling-0 model [21] is appropriate for medium and long-range automotive radar applications where the far-field condition between the sensor and the target is sufficiently satisfied. However, when the target is located within the close range of a high-resolution radar, the received signal is composed of multiple reflections from different parts of the same object [22]. This *extended* target model is more general but has not been considered in any of the previous 802.11ad

978-1-7281-1679-2/19/$31.00 ©2019 IEEE

Authorized licensed use limited to: Indraprastha Institute of Information Technology. Downloaded on July 20,2021 at 12:57:21 UTC from IEEE Xplore. Restrictions apply.

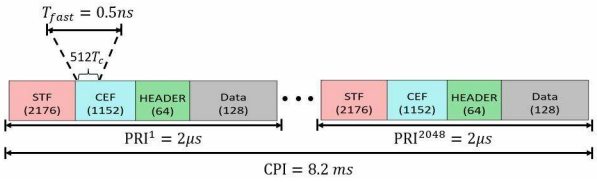

Fig. 2. Proposed Doppler-resilient Golay sequence in the CEF across multiple packets in a coherent processing interval. Consecutive packets contain one member of the Golay pair in the CEF field Gu_{512} that is 512-bit with time interval $T_{fast} = 0.5$ ns. A total of 2048 packets are transmitted.

JRC studies. In this paper, we suggest modifications to the 802.11ad to enable generation of realistic radar signatures of extended targets such as pedestrians as well as large cars.

Prior works [15–17] harness the zero sidelobe attribute of 802.11ad Golay pairs during the matched filtering stage of the radar receiver to estimate the target's location in a delay-Doppler plane. However, the perfect auto-correlation property of Golay pairs holds strictly only for static targets. When the target is moving, the Doppler phase shift in the received signal causes a deterioration in the pulse compression output leading to non-zero side lobes [23]. This effect is accentuated for multiple moving point targets as well as a single extended target with multiple point scatterers moving at different velocities. In order to improve the Doppler tolerance, [23] suggested altering the transmission sequence of Golay pairs.

Unlike previous works, we examine use of Doppler-resilient Golay complementary sequences for extended automotive scatterers, assuming the 802.11ad CEF has embedded in it a complementary pair sequence. In particular, we focus on two common targets. First is a car with four wheels modeled with multiple point scatterers on its body and wheels. The body of the car moves with a fixed translational velocity while the rotational motion of its four wheels introduce micro-Dopplers and micro-range features. The second target is a pedestrian modeled as an extended target with point scatterers on his different body parts. We retrieve the radar signatures from these targets using the standard as well as the proposed Doppler-tolerant 802.11ad protocol. Our results show that we can obtain an improvement of approximately 20 dB in the range side-lobe level when we implement the Doppler resilient protocol as compared to the standard protocol. This property is observed up to a target velocity of ± 144 km/hr.

The paper is organized as follows. In the following section, we describe the signal model of 802.11ad-based radar and introduce the Doppler-resilient link. In Section III, we model the radar back-scatter from the car and pedestrian. We validate our methods through numerical experiments in Section IV and conclude in Section V.

II. Signal Model

The range and Doppler estimation methods using the SCPHY CEF field of standard 802.11ad are described in [15, 17, 20]. In [16], estimation of target parameters using the CPHY frame has been mentioned. In the following, we introduce the radar signal model based on 802.11ad SCPHY that we have adapted for extended targets.

A. Classical 802.11ad-based target localization

A *Golay complementary pair* consists of two unimodular sequences $G_{1,N}$ and $G_{2,N}$ both of the same length N such that the sum of their autocorrelations has a peak of $2N$ and a side-lobe level of zero:

$$G_{1,N}[n] * G_{1,N}[-n] + G_{2,N}[n] * G_{2,N}[-n] = 2N\delta[n]. \quad (1)$$

In previous studies [15–17, 20], the Golay complementary pair members Ga_{256} and Gb_{256} are drawn from the CEF of the same packet (Fig. 1). When these pairs are correlated at the receiver, the pulse repetition intervals (PRIs) for both sequences in the pair differ by a delay equivalent to the transmission time of one 256-bit sequence. Such a non-uniform PRI has a bearing on Doppler estimation but this was ignored in prior works that investigated only macro-Doppler features. To keep the PRI same among all members of the Golay pair, we propose that the complementary sequences are of length 512 and embedded in the Gu_{512} of CEF alternately in two consecutive packets as shown in Fig. 2. For the pth packet, the transmit signal is the 512-bit Golay sequence in CEF:

$$s_T[n] = G_{p,512}[n], \;\; n = 0, 1, \cdots, 511, \quad (2)$$

where $G_{p,512}$ and $G_{(p+1),512}$ are Golay complementary pairs. The discrete-time sequence $s_T[n]$ is passed through a digital-to-analog-converter (DAC) the output of which can be represented as a weighted sum of Dirac impulses:

$$s_T(t) = \sum_{m=0}^{511} s_T[m]\delta(t - mT_c), \quad (3)$$

where $F_c = 1.76$ GHz $= 1/T_c$. This signal is then amplified to impart energy E_s per symbol to the transmit signal. The amplifier output is passed through a transmit shaping filter $h_T(t)$ to obtain

$$x_T(t) = \sqrt{E_s}(s_T * h_T)(t) = \sum_{m=0}^{511} s_T[m]h_T(t - mT_c). \quad (4)$$

The 802.11ad protocol specifies a spectral mask for the transmit signal to limit inter-symbol interference (ISI) [24, section 21.3.2]. We assume that $h_T(t)$ includes a low-pass baseband filter with an equivalent amplitude characteristic of the spectral mask. A common shaping filter has a frequency response $H_T(f)$ of the root raised cosine (RRC) filter [25]. At the receiver, another RRC filter $h_R(t)$ is employed such that the net frequency response is equal to a raised cosine (RC) filter, $H(f) = H_T(f)H_R(f)$. The RC filter is a Nyquist filter with the following time-domain property to avoid ISI:

$$h[n] = h(nT_c) = \begin{cases} 1, & n = 0 \\ 0, & n \neq 0 \end{cases}. \quad (5)$$

We can formulate this as:$h(t) \sum_{k=-\infty}^{+\infty} \delta(t - kT_c) = \delta(t)$. This property only holds for the RC, and not the RRC filter. The baseband signal is then upconverted for transmission: $x(t) = x_T(t)e^{j2\pi f_c t}$, where f_c denotes the carrier frequency. The duration of this transmitted signal is $512T_c = 0.5$ ns and the number of fast time samples is therefore 512. If we assume that the data block consists of 16 Bytes and that there are no optional training fields then each packet is of $T_p = 2$ μs duration which corresponds to the pulse repetition interval.

Assume that the radar transmits P packets constituting one coherent processing interval (CPI) towards a direct-path nonfluctuating extended target of B point scatterers, where a bth point is characterized by complex reflectivity a_b located at range $r_b = c\tau_b/2$ and Doppler $f_{D_b} = \frac{2v_b}{\lambda}$, $c = 3 \times 10^8$ m/s is the speed of light, τ_b is the time delay, v_b is the associated radial velocity and λ is the radar's wavelength. The coefficient a_b subsumes common effects such as antenna directivity, processing gains and attenuations including path loss. Ignoring the multi-path components, the reflected received signal at the baseband, i.e., after down-conversion, is

978-1-7281-1679-2/19/$31.00 ©2019 IEEE

Authorized licensed use limited to: Indraprastha Institute of Information Technology. Downloaded on July 20,2021 at 12:57:21 UTC from IEEE Xplore. Restrictions apply.

$$x_R(t) = \sum_{p=0}^{P-1}\sum_{b=1}^{B} a_b x_T(t-\tau_b-pT_p)e^{-j2\pi f_{D_b} t} + z(t)$$
$$\approx \sum_{p=0}^{P-1}\sum_{b=1}^{B} a_b x_T(t-\tau_b-pT_p)e^{-j2\pi f_{D_b} pT_p} + z(t), \quad (6)$$

where $z(t)$ is additive circular-symmetric white Gaussian noise. The last approximation follows from the fact that $f_{D_b} \ll 1/T_p$ so that the phase rotation within one coherent processing interval (CPI) (*slow time*) can be approximated as a constant. Sampling the signal at $F_c = 1/T_c$ yields $x_R[n] = x_R(nT_c)$:

$$x_R[n] = \sum_{p=0}^{P-1}\sum_{b=1}^{B} a_b x_T(nT_c-\tau_b-pT_p)e^{-j2\pi f_{D_b} pT_p} + z(nT_c)$$
$$= \sum_{p=0}^{P-1}\sum_{b=1}^{B} a_b s_T(nT_c-\tau_b-pT_p)e^{-j2\pi f_{D_b} pT_p} + z[n], \quad (7)$$

where we used Nyquist filter properties (5) in the last equality.

When the sampled signal from two consecutive packets is passed through matched filters of each Golay sequence, we exploit the perfect autocorrelation property to estimate the radar channel. For instance, correlation for the first pair produces

$$\hat{h}_1[n] = x_R[n] * G_{1,512}[-n]$$
$$\hat{h}_2[n] = x_R[n] * G_{2,512}[-n] \quad (8)$$

These outputs are added to return the channel estimate

$$\hat{h}[n] = \frac{1}{1024}(\hat{h}_1[n] + \hat{h}_2[n])$$
$$\approx \frac{1}{1024}\sum_{p=0}^{P-1}\sum_{b=1}^{B} a_b \delta(nT_c-\tau_b-pT_p)e^{-j2\pi f_{D_b} pT_p}$$
$$+ z[n] * (G_{1,512}[-n] + G_{2,512}[-n]), \quad (9)$$

where the last approximation is due to the assumption that the Doppler shifts are nearly identical for the two Golay sequences $G_{1,512}$ and $G_{2,512}$ to utilize the zero side-lobe property of (1). In order to locate the targets in the delay-Doppler plane, the range-time space is discretized into 512 bins of $cT_c/2$ resolution. We then create a delay-Doppler map by taking a 512-point Discrete Fourier Transform (DFT) of the radar channel estimates for each Doppler shift bin. Then, the delay and Doppler frequencies of the point scatterers on the target are given by the location of the B peaks on this 2D delay-Doppler map. For each CPI, the peaks along the Doppler (range) axes for each range (Doppler) bin are coherently summed to obtain the high range resolution profile (Doppler-time spectrogram).

B. Doppler-resilient 802.11ad

When a target is moving, the Doppler shifts across the two waveforms may differ and the approximation in (9) leads to estimation errors in Doppler velocities. A point scatterer moving with a Doppler shift of f_{D_b} gives rise to a phase shift of $\theta \approx 2\pi f_{D_b} T_p$ between $\hat{h}_1$ and $\hat{h}_2$. Then, the perfect autocorrelation no longer holds,

$$\big(G_{1,N}[n] * G_{1,N}[-n]\big) + \big(G_{2,N}[n] * G_{2,N}[-n]\big)\, e^{-j\theta} \neq 2N\delta[n], \quad (10)$$

resulting in high side-lobes along the range. For example, consider a scatterer at (r_b = 20 m,v_b = 10 m/s) over 1 CPI of P = 2048 packets. For this set of waveform parameters, Fig. 3a plots the *ambiguity function* (AF) obtained by correlating the waveform with its Doppler-shifted and delayed replicas. The AF completely characterizes the radar's ability to discriminate in both range and velocity of its transmit waveform. The complementary Golay AF shows a very high sidelobe level of -20 dB at non-zero Doppler frequencies. This would result in poor detection of moving extended targets wherein strong scatterer points masks the weaker ones. It is difficult to ascertain the high resolution micro-Doppler features of such a target.

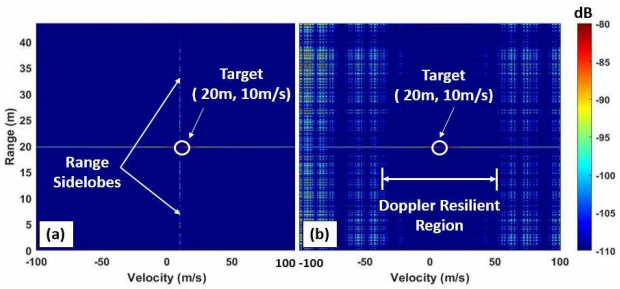

Fig. 3. Ambiguity function for a point scatterer at range 20 m and moving at 10 m/s using (a) standard Golay (b) Doppler resilient Golay waveform.

The limitation described above can be overcome by using Doppler-tolerant Golay sequences such as the one proposed in [23]. Without loss of generality, assume P be even and generate the Prouhet-Thue-Morse (PTM) sequence [26], $\{q_p\}_{p=0}^{\frac{P}{2}-1}$ which takes values in the set $\{0,1\}$ through following Boolean recursion:

$$q_p = \begin{cases} 0, & \text{if } p = 0 \\ q_{\frac{p}{2}}, & \text{if } (p \text{ modulo } 2) = 0 \\ \overline{q_{\frac{p-1}{2}}}, & \text{if } (p \text{ modulo } 2) = 1, \end{cases} \quad (11)$$

where $\overline{q_p}$ denotes the binary complement of q_p. As an example, when $P = 16$, the PTM sequence is $q_0 = \{0,1,1,0,1,0,0,1\}$.

Based on the values of q_p, we transmit the following Golay pairs: if $q_1 = 0$, then the complementary pair $G_{1,N}[n]$ and $G_{2,N}[n]$ are transmitted separately in two consecutive packets; if $q_2 = 1$, then the consecutive transmission consists of the complementary pair with $-G_{2,N}[-n]$ and $G_{1,N}[-n]$; and so on. In this manner, we transmit a sequence of Doppler-resilient Golay sequences over P packets. The goal is to obtain a pulse train of Golay pairs such that

$$\sum_{p=0}^{P-1} e^{jn\theta}(G_{p,N}[n] * G_{p,N}[n]) \approx f(\theta)\delta[n], \quad (12)$$

where the function $f(\theta)$ does not depend on the time-shift index n for some reasonably large values of θ. The Taylor series approximation of the left-hand-side of (12) around zero Doppler is

$$\sum_{p=0}^{P-1} e^{jn\theta}(G_{p,N}[n] * G_{p,N}[n]) \approx 0(G_{0,N}[n] * G_{0,N}[n])$$
$$+ 1(G_{1,N}[n] * G_{1,N}[n]) + 2(G_{2,N}[n] * G_{2,N}[n])$$
$$+ \cdots + (P-1)(G_{P-1,N}[n] * G_{P-1,N}[n]). \quad (13)$$

Using PTM sequence, the above summation can be made to approach a delta function. The key is to transmit a Golay sequence that is also complementary with sequences in more than one packet.

For these Doppler-resilient Golay sequences, the resultant AF plot is nearly free of range sidelobes especially at low Doppler velocities as shown in Fig.3. The range slice in Fig.4(a),(b) show the 20dB reduction in sidelobe levels.

978-1-7281-1679-2/19/$31.00 ©2019 IEEE

Authorized licensed use limited to: Indraprastha Institute of Information Technology. Downloaded on July 20,2021 at 12:57:21 UTC from IEEE Xplore. Restrictions apply.

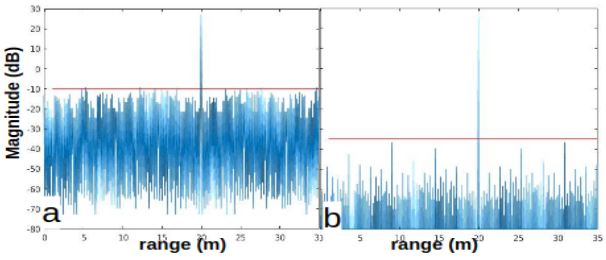

Fig. 4. The range slices of the ambiguity functions in Fig. 3(a),(b) at velocity = 10m/s show the 20dB reduction in side lobe level

III. Target Models

We consider modeling two classes of automotive targets - large cars and pedestrians. Both are complex three-dimensional dynamic targets. In a car, the motion of four wheels produces micro-motion features in the radar signature. For a pedestrian, the swinging motion of the arms and legs generates micro-Doppler and micro-range tracks. The backscatter from these targets can be accurately modeled using full wave electromagnetic solvers such as method of moments (MoM) or finite element method (FEM). However, the electric size of the problem becomes very large at mmWave frequencies and it is not feasible to use these techniques to generate radar data across multiple frames at high sampling frequencies. Therefore, we simulate the backscatter by modeling cars and pedestrians as extended targets with multiple point scatterers, $\{u_l\}_{l=1}^{U_l}$, distributed across the target's body. Thereafter, we obtain the time-domain trajectories of the positions of these scatterers via either computer animations [27] or analytical models [28]. As noted in (7), The overall backscatter from the target is the sum of the complex-valued returns from each of these scatterers.

The above-mentioned technique has been extensively used to model radar signatures of humans at microwave frequencies [29]. The resultant micro-Doppler and high range resolution profiles were found to be qualitatively comparable with those obtained from the measured data. We adopt this approach to generate radar signatures of cars and pedestrians using both standard and Doppler resilient Golay codes for the transmit waveforms. This simulation method is not without its limitations. For example, it does not yield accurate estimations of the radar cross-sections of a target. Further, it assumes Born approximation [30] and cannot be used to model multiple scatterers and shadowing between different parts of the target.

In case of a car, we generate the backscatter by combining a realistic animation model with the point scatterer simulation technique discussed above. We model the car as a rigid body in pyBullet software [31]. used for physics simulation of vehicles. We structured the car using rigid bodies such as a cuboid for the chassis, cylinders for the wheels, and so on. The interiors of the car were represented using three-dimensional models of gears and other mechanical assemblies. Key components of this model are the Ackermann steering [32] and automotive differential [33] guiding the motions of the four wheels along different trajectories. We used following parameters in our simulation: wheel axle length of 2 m, front axle to rear axle length of 3.5 m, wheel radius of 0.48 m. These values correspond to large cars. We considered 44 point scatterers - 1 on each of the axle ends and 10 each on the four wheels of the car (Fig. 5a). When the car moves, the chassis of the car moves at a translational velocity, $\vec{v}_{axle}$. The wheels, on the other hand, have an additional rotational velocity. As a result, the point scatterers on the wheels move along a cycloidal curve with respect to the radar. The position $\vec{p}_l(t)$ of the l^{th} point scatterer on the wheel is

$$\vec{p}_l(t) = \vec{p}_l^{\,0} + \vec{v}_{axle}t + r_{wheel}\left(\vec{\omega_r} \times \begin{bmatrix} \cos\left(|\vec{\omega_r}|t + \phi_l\right) \\ 0 \\ -\sin\left(|\vec{\omega_r}|t + \phi_l\right) \end{bmatrix}\right) t, \quad (14)$$

where $\vec{\omega_r}$ is the angular velocity of the r^{th} wheel, ϕ_l is the starting phase corresponding to the position of the l^{th} point scatterer on the wheel, r_{wheel} is the radius of the wheel and $\vec{p}_l^{\,0}$ is the initial position of the point scatterer. When the car moves in a straight line, all the four wheels have identical angular velocities. The trajectory of the point scatterers on the wheels depend on the position of each wheel with respect to the radar. Therefore, each wheel has a unique velocity-time trajectory. In this work, we consider two scenarios shown in Fig. 5b and c. The first scenario has the car starting acceleration from 0 m/s to 4 m/s as it moves away from the radar along a straight path. In the second, the car moves with a constant speed along the transverse direction with respect to the radar. The first scenario represents the case where the radar is tracking a car moving ahead on the same lane whereas the second represents the scenario where the car is moving in a lateral direction at a traffic junction.

To simulate the backscatter from a pedestrian, we employ the analytical model from [28] to describe the time-domain trajectories of seventeen point scatterers on a human body moving at a constant velocity. The point scatterers are distributed across the head, torso, arms and legs as shown in Fig. 6a. We consider a human of height 1.5 m walking at a speed of 1.5 m/s. We consider two trajectories of the pedestrian motion that may be commonly encountered in an automotive scenario: pedestrian walking along a straight line towards the radar (Fig. 6b), and walking along a transverse direction with respect to the road (Fig. 6c).

Typically, the reflectivities of the point scatterers change with time due to variations in the orientation of different body parts with respect to the radar. This is in accordance with the Swerling I target model [34]. In our work, we are interested in the detailed features in the target's signature rather than the scale of the resulting radar cross-section. Hence, the reflectivities from all the point scatterers are unity.

IV. Numerical Experiments

We validated our proposed Doppler-resilient 802.11ad through numerical experiments. For each automotive target and waveform, we compared the signature on the radar in three joint domains: range-time, Doppler-time spectrograms and range-Doppler-time signatures for the automotive targets. We used a Nvidia 1080-TI GPU with CUDA 9.0 for processing the data in MATLAB R2018a, Parallel Processing Toolbox environment. We generated the range-Doppler signatures for a given CPI by following the signal model in Section II. For the Doppler-time (range-time) spectrograms, we coherently integrated the peaks from all the range (Doppler) bins in each time-frame.

Large car (straight trajectory): Figure 7 shows the backscatter signatures of the car moving along a straight line trajectory away from the radar. The relative locations of the radar with respect to the target is shown in Fig. 5. In Fig. 7a, as the car moves away from the radar (evident from the increasing range), we see multiple tracks corresponding to the wheels on two sides of the car. The quality of the range-time display obtained from standard Golay sequences (Fig. 7a) is significantly poorer than the Doppler-resilient Golay (Fig. 7d) because of the presence of high range side-lobes (visible in the background starting from 1.5 s). These side-lobes significantly impact the detection of weaker targets in the presence of strong ones. The trajectories of the multiple point scatterers on the wheels can be observed in the Doppler-time plane shown in Figs. 7b and e. The point on the wheel that is in contact with the ground moves with zero velocity while the point on the top of the wheel moves with maximum velocity which corresponds to twice the instantaneous linear velocity of the car. All other points on the wheel move with intermediate velocities Therefore, the Doppler tracks range from 0 Hz to the maximum over each rotation cycle of the wheel. The Doppler-time signatures obtained from both standard 802.11ad and Doppler resilient Golay are similar. In other words, the perturbation in the perfect auto-correlation property affects only the range measurements. We

978-1-7281-1679-2/19/$31.00 ©2019 IEEE

Authorized licensed use limited to: Indraprastha Institute of Information Technology. Downloaded on July 20,2021 at 12:57:21 UTC from IEEE Xplore. Restrictions apply.

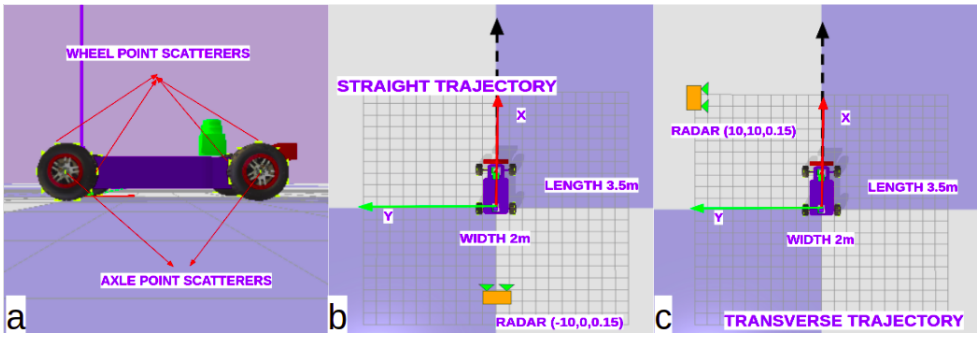

Fig. 5. (a) Point scatterer model of car. Trajectories of car with respect to the radar: (b) Car accelerating directly in line away from the radar (c) Car moving with a fixed velocity in a transverse direction in front of a radar.

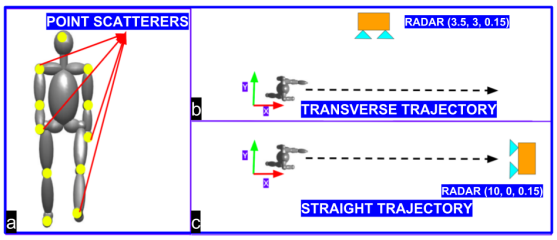

Fig. 6. (a) Point scatterer model of a pedestrian. Trajectories of pedestrian motion with respect to the radar: (b) Human walking in a transverse direction before a radar (c) Human walking directly in line towards the radar.

now examine a single frame of the target's signature in the range-Doppler plane (Figs. 7c and f). Here, multiple point scatterers at different ranges and velocities are convolved with the point spread response along the two axes. We note that the high range-sidelobes seen in the standard Golay signatures are suppressed by 20 dB in Doppler-resilient signatures.

Large car (transverse trajectory): Hereafter, we limit our analyses to the signatures generated from only Doppler-resilient Golay sequences. The range gradually decreases as the car approaches the radar transversely, reaches a minimum value when the car is immediately before the (stationary) radar, and increases as the car moves away. This phenomenon is observed in the range-time signature shown in Fig. 8a. The Doppler spectrogram of the car making a transverse path shows some interesting features in Fig. 8b. The Doppler reduces to zero when the car is directly before the radar since the radial component of the velocity vanishes. At other points in its trajectory, we see a wide spectrum of velocities from the multiple scatterers on the wheels. The velocities are positive (negative) when the car approaches (moves away from) the radar.

Pedestrian: Figure 9 shows signatures of a walking pedestrian generated using Doppler-resilient Golay sequences. Even though a pedestrian is an extended target, the radar range resolution is not fine enough for us to be able to observe distinct tracks from the different point scatterers in the range-time signatures of both straight (Fig. 9a) and transverse (Fig. 9c) trajectories of the pedestrian. On the other hand, the corresponding Doppler spectrograms (Figs. 9b and d) exhibit Doppler-time tracks of individual point scatterers. The maximum Dopplers are due to the motion of the feet followed by the hands and the torso. For a pedestrian walking towards a radar along a straight line, the micro-Dopplers are mostly positive. However, when the pedestrian motion is along a lateral direction, the Dopplers are positive during the first few seconds as the target walks towards the radar and then negative when the pedestrian moves away.

V. Summary

We presented a 802.11ad link that can be used for generating detailed radar signatures for different types of automotive targets. The existing preamble of the link consists of Golay complementary sequences that are characterized by perfect autocorrelation properties for static targets. In

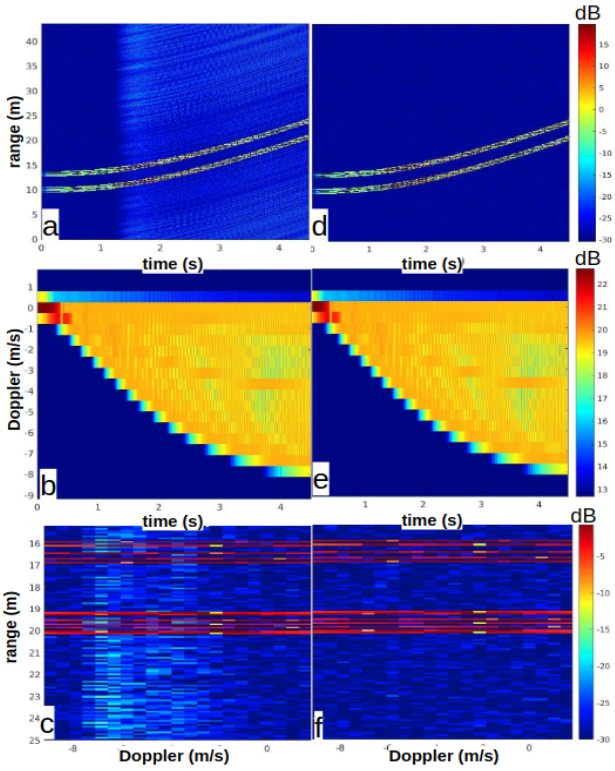

Fig. 7. Range-time (a,d), Range (b,e) and range-Doppler (c,f) signatures of a large car moving in a straight path using standard Golay sequence (a to c) and Doppler resilient Golay sequences (d to f). Fig. 5b shows the relative location of the radar with respect to the car.

case of multiple moving targets or a single extended target with multiple moving point scatterers, the Doppler phase shift causes perturbation in the perfect autocorrelation and introduces range side-lobes. We demonstrated that by modifying the 802.11.ad Golay waveform with a specific pulse train sequence to reduce the side-lobes by 20 dB, realistic detection of modest Doppler shifts corresponding to typical automotive scenario velocities is possible. We presented radar signatures of a large car and a pedestrian using these modified sequences and compared them with the signatures obtained from the standard 802.11ad Golay sequences.

Acknowledgment

G. D. and S. S. R. were funded by Air Force Office of Scientific Research (AFOSR), AOARD through the 5IOA036 FA23861610004 grant. We would like to acknowledge Dr. Aman Parnami of the Weave

978-1-7281-1679-2/19/$31.00 ©2019 IEEE

Authorized licensed use limited to: Indraprastha Institute of Information Technology. Downloaded on July 20,2021 at 12:57:21 UTC from IEEE Xplore. Restrictions apply.

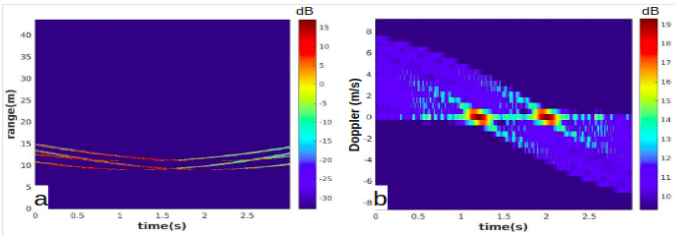

Fig. 8. (a) Range-time and (b) Doppler-time signatures of a large car moving in a transverse path using Doppler resilient Golay sequence. Fig. 5c shows the relative location of the radar with respect to the car.

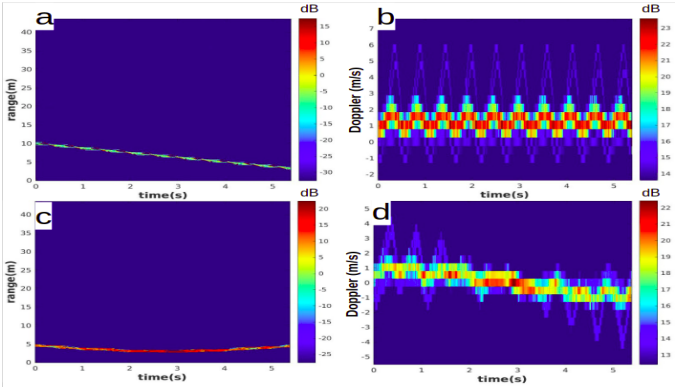

Fig. 9. Range-Time (a,c) and Doppler-time (b,d) signatures of a human moving in a straight (a-b) or transverse path (c-d) using Doppler resilient Golay sequences. Fig. 6b-c shows the relative location of the radar with respect to the pedestrian.

Lab IIITD for providing a high-performance GPU-based server. K. V. M. was supported by Iowa Flood Center.

REFERENCES

[1] K. Bengler, K. Dietmayer, B. Farber, M. Maurer, C. Stiller, and H. Winner, "Three decades of driver assistance systems: Review and future perspectives," *IEEE Intelligent Transportation Systems Magazine*, vol. 6, no. 4, pp. 6–22, 2014.

[2] J. Funke, M. Brown, S. M. Erlien, and J. C. Gerdes, "Collision avoidance and stabilization for autonomous vehicles in emergency scenarios," *IEEE Transactions on Control Systems Technology*, vol. 25, no. 4, pp. 1204–1216, 2017.

[3] L. Kong, M. K. Khan, F. Wu, G. Chen, and P. Zeng, "Millimeter-wave wireless communications for IoT-cloud supported autonomous vehicles: Overview, design, and challenges," *IEEE Communications Magazine*, vol. 55, no. 1, pp. 62–68, 2017.

[4] K. V. Mishra, A. Zhitnikov, and Y. C. Eldar, "Spectrum sharing solution for automotive radar," in *IEEE Vehicular Technology Conference - Spring*, 2017, pp. 1–5.

[5] M. Gerla, E.-K. Lee, G. Pau, and U. Lee, "Internet of vehicles: From intelligent grid to autonomous cars and vehicular clouds," in *IEEE World Forum on Internet of Things*, 2014, pp. 241–246.

[6] C. Premebida, O. Ludwig, and U. Nunes, "LIDAR and vision-based pedestrian detection system," *Journal of Field Robotics*, vol. 26, no. 9, pp. 696–711, 2009.

[7] F. Xu, X. Liu, and K. Fujimura, "Pedestrian detection and tracking with night vision," *IEEE Transactions on Intelligent Transportation Systems*, vol. 6, no. 1, pp. 63–71, 2005.

[8] L. Li, F. Zhou, and X. Bai, "Infrared pedestrian segmentation through background likelihood and object-biased saliency," *IEEE Transactions on Intelligent Transportation Systems*, no. 99, pp. 1–19, 2017.

[9] A. Angelov, A. Robertson, R. Murray-Smith, and F. Fioranelli, "Practical classification of different moving targets using automotive radar and deep neural networks," *IET Radar, Sonar & Navigation*, vol. 12, pp. 1082–1089, 2018.

[10] S. Björklund, H. Petersson, A. Nezirovic, M. B. Guldogan, and F. Gustafsson, "Millimeter-wave radar micro-Doppler signatures of human motion," in *IEEE International Radar Symposium*, 2011, pp. 167–174.

[11] V. C. Chen, "Analysis of radar micro-Doppler with time-frequency transform," in *IEEE Workshop on Statistical Signal and Array Processing*, 2000, pp. 463–466.

[12] J. Hasch, E. Topak, R. Schnabel, T. Zwick, R. Weigel, and C. Waldschmidt, "Millimeter-wave technology for automotive radar sensors in the 77 GHz frequency band," *IEEE Transactions on Microwave Theory and Techniques*, vol. 60, no. 3, pp. 845–860, 2012.

[13] J. Harding, G. Powell, R. Yoon, J. Fikentscher, C. Doyle, D. Sade, M. Lukuc, J. Simons, and J. Wang, "Vehicle-to-vehicle communications: Readiness of V2V technology for application," National Highway Traffic Safety Administration, Tech. Rep. DOT HS 812 014, 2014.

[14] T. Nitsche, C. Cordeiro, A. B. Flores, E. W. Knightly, E. Perahia, and J. C. Widmer, "IEEE 802.11ad: Directional 60 GHz communication for multi-Gigabit-per-second Wi-Fi," *IEEE Communications Magazine*, vol. 52, no. 12, pp. 132–141, 2014.

[15] P. Kumari, N. González-Prelcic, and R. W. Heath Jr., "Investigating the IEEE 802.11ad standard for millimeter wave automotive radar," in *IEEE Vehicular Technology Conference - Spring*, 2015, pp. 1–5.

[16] E. Grossi, M. Lops, L. Venturino, and A. Zappone, "Opportunistic radar in IEEE 802.11ad networks," *IEEE Transactions on Signal Processing*, vol. 66, no. 9, pp. 2441–2454, 2018.

[17] G. R. Muns, K. V. Mishra, C. B. Guerra, Y. C. Eldar, and K. R. Chowdhury, "Beam alignment and tracking for autonomous vehicular communication using IEEE 802.11ad-based radar," in *IEEE Infocom Workshops - Hot Topics in Social and Mobile Connected Smart Objects*, 2019, in press.

[18] I. Mavromatis, A. Tassi, R. J. Piechocki, and A. Nix, "Beam alignment for millimetre wave links with motion prediction of autonomous vehicles," in *IET Colloquium on Antennas, Propagation & RF Technology for Transport and Autonomous Platforms*, 2017, pp. 1–8.

[19] M. J. E. Golay, "Complementary series," *IRE Transactions on Information Theory*, vol. 7, no. 2, pp. 82–87, 1961.

[20] K. V. Mishra and Y. C. Eldar, "Sub-Nyquist channel estimation over IEEE 802.11ad link," in *IEEE International Conference on Sampling Theory and Applications*, 2017, pp. 355–359.

[21] P. Swerling, "Probability of detection for fluctuating targets," *IRE Transactions on Information Theory*, vol. 6, no. 2, pp. 269–308, 1960.

[22] S. H. Dokhanchi, M. R. Bhavani Shankar, K. V. Mishra, and B. Ottersten, "A mmWave automotive joint radar-communication system," *IEEE Transactions on Aerospace and Electronic Systems*, 2019, in press.

[23] A. Pezeshki, A. R. Calderbank, W. Moran, and S. D. Howard, "Doppler resilient Golay complementary waveforms," *IEEE Transactions on Information Theory*, vol. 54, no. 9, pp. 4254–4266, 2008.

[24] *Wireless LAN Medium Access Control (MAC) and Physical Layer (PHY) Specifications Amendment 3: Enhancements for Very High Throughput in the 60 GHz Band*, 2012, IEEE Std. 802.11ad.

[25] A. F. Molisch, *Wireless communications*. John Wiley & Sons, 2012.

[26] J. P. Allouche and J. Shallit, "The ubiquitous Prouhet-Thue-Morse sequence," in *Sequences and Their Applications*, T. H. C. Ding and H. Niederreiter, Eds. Springer-Verlag, 1999.

[27] A. D. Singh, S. S. Ram, and S. Vishwakarma, "Simulation of the radar cross-section of dynamic human motions using virtual reality data and ray tracing," in *IEEE Radar Conference*, 2018, pp. 1555–1560.

[28] V. C. Chen, F. Li, S.-S. Ho, and H. Wechsler, "Micro-Doppler effect in radar: Phenomenon, model, and simulation study," *IEEE Transactions on Aerospace and Electronic Systems*, vol. 42, no. 1, pp. 2–21, 2006.

[29] S. S. Ram and H. Ling, "Simulation of human microDopplers using computer animation data," in *IEEE Radar Conference*, 2008, pp. 1–6.

[30] M. Cheney and B. Borden, *Fundamentals of radar imaging*, ser. CBMS-NSF Regional Conference Series in Applied Mathematics. SIAM, 2009, vol. 79.

[31] E. Coumans and Y. Bai, "PyBullet quickstart guide," https://pythonhosted.org/pybullet/, 2017-2018.

[32] S. Chocholek, "The development of a differential for the improvement of traction control," in *International Conference on Traction Control and Anti Wheel Spin Systems for Road Vehicles*, 1988, pp. 75–82.

[33] W. Norris, *Modern steam road wagons*. Longmans, Green, and co., 1906.

[34] M. I. Skolnik, *Radar handbook*, 3rd ed. McGraw-Hill, 2008.

978-1-7281-1679-2/19/$31.00 ©2019 IEEE

Authorized licensed use limited to: Indraprastha Institute of Information Technology. Downloaded on July 20,2021 at 12:57:21 UTC from IEEE Xplore. Restrictions apply.